JOURNAL OF SOLID STATE CHEMISTRY 16, 331–347 (1976)

High-Temperature Rutile-Derived Crystallographic Shear Structures. I. $(020)_r$ *CS* Structures

L. A. BURSILL

Physics Department, University of Melbourne, Parkville, Victoria 3052, Australia

I. E. GREY

CSIRO Division of Mineral Chemistry, P.O. Box 124, Port Melbourne, Victoria 3207, Australia

AND D. J. LLOYD

Chemistry Department, Monash University, Clayton, Victoria 3168, Australia

Received April 22, 1975

Electron diffraction and single-crystal X-ray diffraction techniques have been applied to a study of the structures of phases in the Fe_2O_3–TiO_2 system, for compositions in the range 14–16 wt% Fe_2O_3 and for temperatures above 1450°C. The compounds in this system may be described as $(020)_r$ *CS* phases in which adjacent rutile slabs, infinitely extended along $[100]_r$ and $[001]_r$, are displaced by $\frac{1}{2}[011]_r$ across $(020)_r$ *CS* planes. In the *CS* planes, about two-thirds of the available metal-atom octahedral sites are occupied in a deficient NiAs arrangement. The composition range studied is spanned by a continuous series of $(020)_r$ intergrowths formed by the ordered mixing of structures with two different *CS* plane spacings, namely, $9 \times d_{(020)_r}$ and $11 \times d_{(020)_r}$.

Conventional structure solution methods could not be applied to these infinitely adaptive structures because of the small intensity data to parameter ratios for the high-order intergrowths. We describe a method of structure solution based on a series of successive approximations. The method was applied to determine the structure of one of the intergrowths using single-crystal X-ray diffraction data.

For the temperature range studied, the *CS* phases are within a few degrees of their melting points, and this is reflected in a departure from complete structural order. The results show both long-range disorder in the intergrowth sequences and an absence of correlation between the metal-atom ordering in one *CS* plane and the next. This disorder is manifested by diffuse scattering in the diffraction patterns.

The $(020)_r$ *CS* structures transform reversibly to the well-known $(121)_r$–$(132)_r$ family of ordered rutile *CS* structures below 1450°C.

1. Introduction

Recently we discovered rutile-derived *CS* structures in the system TiO_2 plus 0–13 wt% Fe_2O_3 (*1*). As in the $(Ti^{4+}, Ti^{3+})O_x$ and $(Ti^{4+}, Cr^{3+})O_x$ systems in certain stoichiometry ranges, the *CS* plane indices $(hkl)_r$ pivoted from $(132)_r$ to $(121)_r$, where $(hkl)_r = p\cdot(121)_r + q\cdot(011)_r$ (*2*). All of these *CS* planes lie in the $[1\bar{1}1]_r$ zone, and all have the idealized displacement vector $\frac{1}{2}[0\bar{1}1]_r$. However, in the case of the iron-doped rutile system, we found a new superstructure with a long period which appeared to be normal to the (010) planes of

rutile. It occurred only in preparations heated above 1450°C.

High-temperature phase analysis studies, using electron microscopy/diffraction combined with powder and single-crystal X-ray diffraction techniques, have now revealed that the ordered $(hkl)_r$ *CS* structures undergo a reversible structural transformation at about 1450°C. This involves a new cooperative reorientation of the *CS* planes away from the $[1\bar{1}1]_r$ zone into the more symmetrical $[100]_r$ zone. In these high-temperature structures, compositional changes are effected by both "swinging" of the *CS* planes within the $[100]_r$ zone, and by changing the average *CS* plane spacing. The former predominates in the approximate composition range 8–13 wt% Fe_2O_3 where, with increasing Fe_2O_3 content, the *CS* plane swings from $(031)_r$ to $(020)_r$. Above about 13 wt% Fe_2O_3 we find a quasi-continuous series of parallel intergrowths of $(020)_r$ structures. A brief report of these new *CS* structures was given at a recent conference (*3*).

As a first step toward determining the crystal structures of the high temperature phases we undertook a single crystal X-ray structure determination on a crystal having a $(020)_r$ superstructure. This study is reported below.

2. Experimental

2.1. Specimen Preparation

Crystals displaying $(020)_r$ superstructures were prepared at 1500–1550°C by reacting $Fe_2O_3 + TiO_2$ mixtures with Fe/Ti ratios greater than 0.15 (i.e., greater than 13 wt% Fe_2O_3). Pressed pellets of the mixtures were equilibrated in air or in oxygen for about 20 hr and then rapidly quenched. Reaction for longer periods resulted in some loss of iron from the mixtures by volatilization. X-ray powder diffraction patterns showed predominantly the high-temperature phase, together with some pseudobrookite. This is consistent with MacChesney and Muan's work (*4*) on the iron titanium oxide system in air at 1500°C. They show a rutile "solid solution" extending to 85% TiO_2, beyond which pseudobrookite appears. Their phase analysis also showed that Fe_2O_3 is unstable relative to Fe_3O_4 in air at 1500°C, i.e., we are dealing with the ternary system $FeO + Fe_2O_3 + TiO_2$. Attempts to determine the Fe^{2+}/Fe^{3+} ratio in the rutile *CS* phases by chemical analysis were not successful owing to the extreme insolubility of the materials, even in heated HF/H_2SO_4 mixtures. However, application of the Mössbauer technique proved successful; ferric and ferrous iron gave separate, easily distinguishable quadrupole doublets. Spectra were run on a number of samples prepared in air at 1500°C. In all cases the ferrous iron content was very low, i.e., less than 5 wt% of the total iron. The reaction products were in the form of sintered aggregates of deep red-brown crystallites which appeared shiny-black by reflected light. Slight crushing broke the sinter into well-defined crystals of average linear dimensions 0.1–0.2 mm. In some preparations, where the temperature was higher than 1500°C, some of the material had melted. MacChesney and Muan's phase diagram shows the rutile "solid solution" to be in equilibrium with a liquid phase above 1515°C.

2.2. Electron Diffraction

Thin fracture fragments suitable for transmission electron microscopy were obtained by crushing. These were dispersed on carbon support films. $[111]_r$, $[101]_r$, $[100]_r$, $[010]_r$, and $[001]_r$ zone axis diffraction patterns were obtained for the superstructures using a JEM-7 electron microscope fitted with a goniometer stage.

2.3. X-Ray Diffraction

A number of crystals prepared as described above were initially examined using Weissenberg and precession techniques to check if they were single phase and free from twinning. One such fragment, a small columnar crystal of approximate dimensions 0.05 × 0.05 × 0.15 mm, mounted about the column axis, was selected as being apparently suitable for a single crystal study. The data were collected with Mo$K\alpha$ radiation using a Philips PW1100 automatic diffractometer with a graphite monochromator.

Initial attempts to define a unit cell on the basis of 25 reflections found in a search were unsuccessful because of spacing anomalies that existed in the lattice. However, the reflections were indexed satisfactorily by imposing a unit cell which had been obtained by least-squares refinement of powder diffraction data, and then all reflection positions could be calculated with reasonable precision. For data collection, a scan rate of $0.1°\ \text{sec}^{-1}$ was used in the $\theta/2\theta$ mode over a range about the calculated scattering position given by the expression $(0.8 + 0.3\tan\theta)$ degrees. In the occasional case of interfering reflections, manual optimization was used to obtain a faithful intensity measurement.

The intensities were processed using a program written for the PW1100 diffractometer by Hornstra and Stubbe (*5*). The standard deviation of each net intensity was assigned according to the formula

$$\sigma(I) = [CT + (t_c/t_b)^2(B1 + B2) + (pI)^2]^{1/2},$$

where CT is the total integrated peak count obtained in a scan time t_c, $B1$ and $B2$ are background counts each obtained in time t_b, and

$$I = CT - (t_c/t_b)(B1 + B2).$$

The value of p, the term used to prevent unrealistically high weights being assigned to strong reflections, was selected as 0.04.

The values of I and $\sigma(I)$ were then corrected for Lorentz and polarization effects in the normal manner, but were not corrected for either absorption or extinction effects. Of 1301 independent reflections, 451 with $F^2 > 2\sigma(F^2)$ were used in the structure determination.

3. Observations

Electron diffraction patterns for the high temperature structures display a pronounced rutile subcell with superstructure reflections directed along one of the tetragonal a^* directions. In Figs. 1a–c are shown $[100]_r$, $[100]_r$, and $[001]_r$ zone axis diffraction patterns for three different single-crystal flakes. The superperiods are 10.7, 9.6, and $10.4 \times d_{(020)_r}$, respectively. In fact, the $[001]_r$ zone was obtained much more readily than other zones. The superperiod was usually a nonintegral multiple of $d_{(020)_r}$, despite the fact that there was always a spot in the $(020)_r$ position. A possible explanation for the observed spacing anomalies is that the rows of superlattice spots are *inclined* to the $(001)_r$ reciprocal lattice plane, being directed along the reciprocal lattice vector $\mathbf{g}(0kl)_r$ rather than $\mathbf{g}(020)_r$, and that we are merely observing a projection of the true reciprocal lattice rows, due to spiking of diffraction spots, for thin crystals, in the direction of the electron beam. It is often difficult to check this effect on a particular fragment being examined by electron diffraction, owing to the restricted tilt range ($\pm 30°$ in this case). In X-ray studies, using the precession method, a single crystal may be oriented to study *any* desired reciprocal sections. A large number of crystals were thus examined by both the X-ray precession method and by electron diffraction. Eventually it became clear that for preparations containing greater than about 13 wt% Fe_2O_3 the superlattice was in fact along $\mathbf{g}(020)_r$ and that for these crystals there was indeed a continuous range of superlattice spacings from 9.6 to $11 \times d_{(020)_r}$ (i.e., 22.4–25.7 Å). To identify these reflections, we must first obtain the $[100]_r$ zone, which contains all of the $(0kl)_r$ planes (e.g., Figs. 1a, b, and d). On the other hand, for preparations containing 8–13 wt% Fe_2O_3, single-crystal diffraction patterns showed that the direction of the superlattice rows swings away from $(020)_r$, through $(061)_r$, $(041)_r$ to $(031)_r$ as higher oxygen/metal ratios were examined. An example of the $(031)_r$ superstructure is shown in Fig. 1d, which shows the same $[100]_r$ zone as Fig. 1b; now, the superlattice rows run parallel to $\mathbf{g}(031)_r$ and $\mathbf{g}(03\bar{1})_r$.

3.1. Diffuse Scattering

For certain reciprocal lattice sections, diffuse scattering was a prominent feature of the electron diffraction patterns. Starting with a $[001]_r$ zone diffraction pattern (cf. Fig. 1c) and tilting about $[010]_r$ gave patterns (Fig. 2a) showing diffuse streaks elongated parallel to $\mathbf{g}(020)_r$. The superlattice spacing, 25.9 Å along $\mathbf{g}(020)_r$ in Fig. 2a, lies at the end of the range

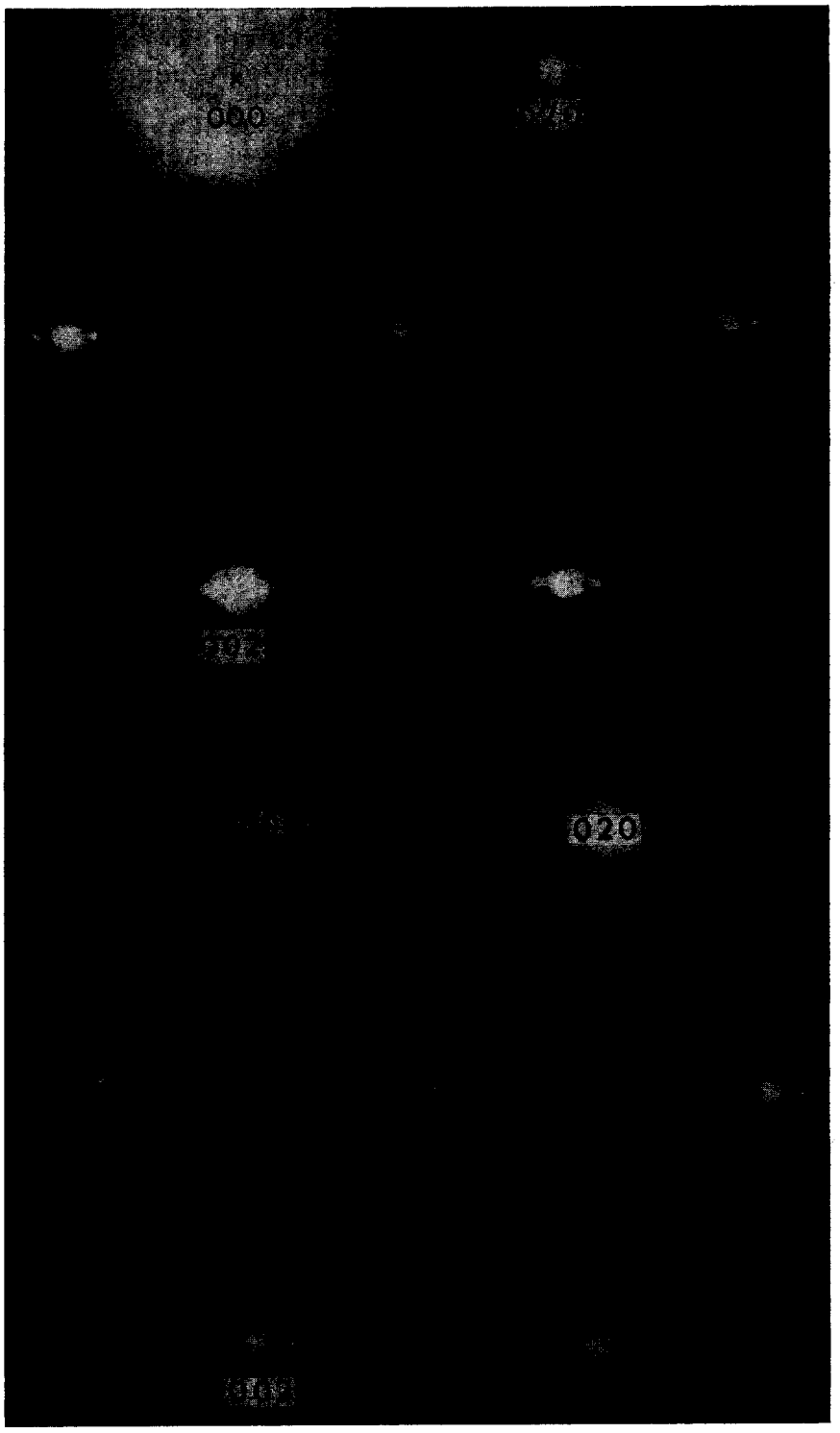
000
020

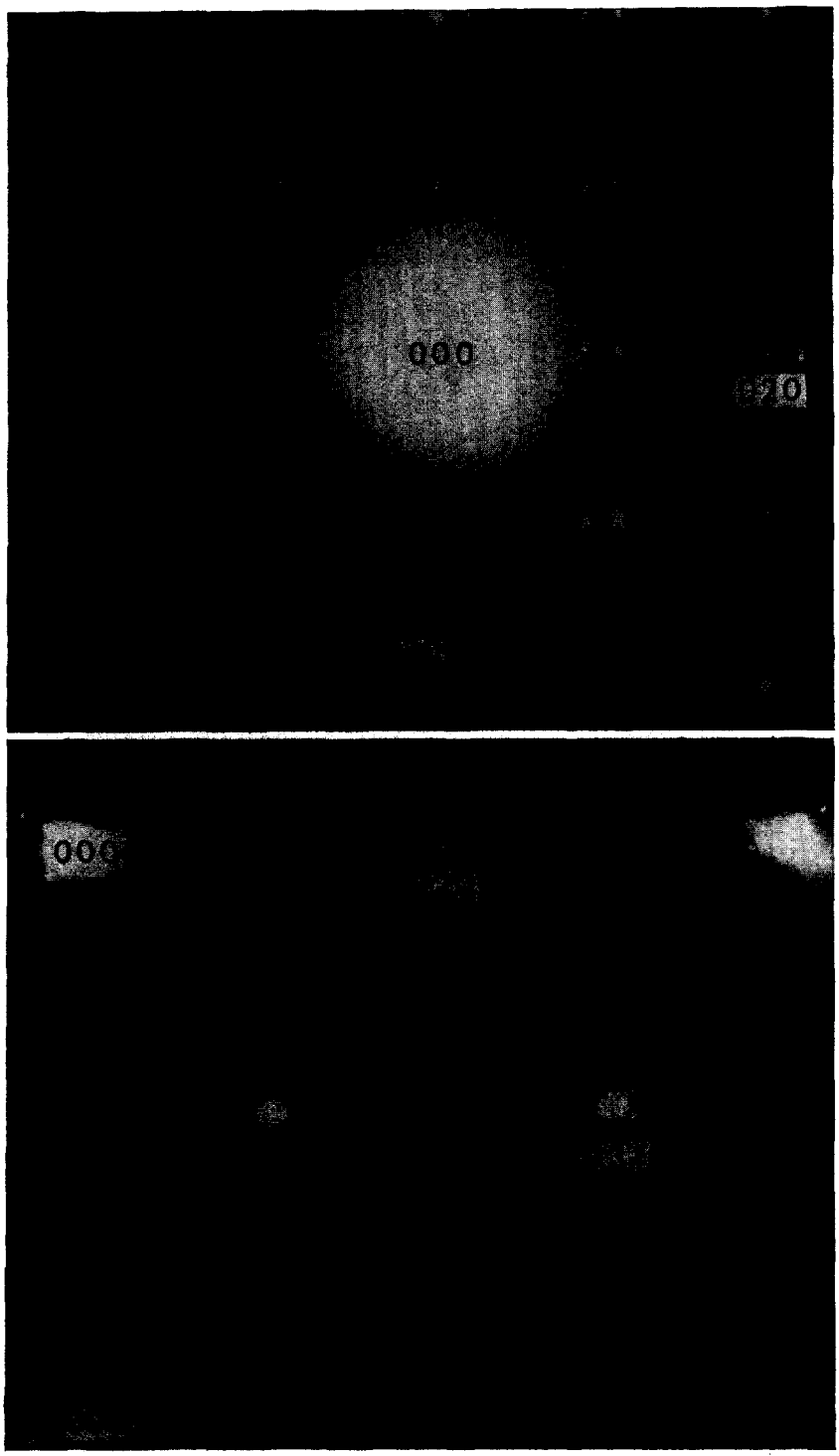

FIG. 1. Selected area electron diffraction patterns for (020)$_r$ superstructures (a, b, c) and an (031)$_r$ superstructure (d): (a), (b), (d), [100]$_r$ zone axis patterns; (c), [001]$_r$ zone axis pattern.

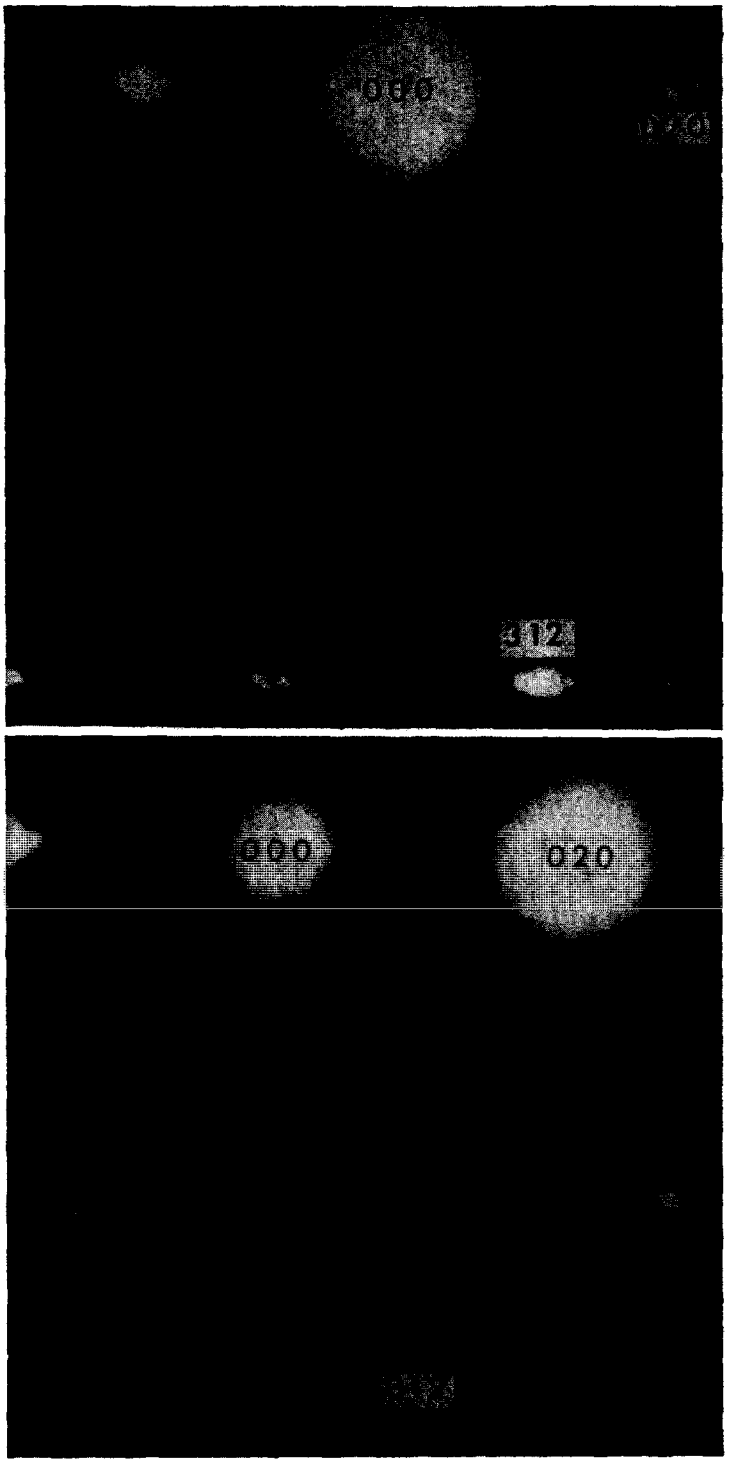
020
020
020

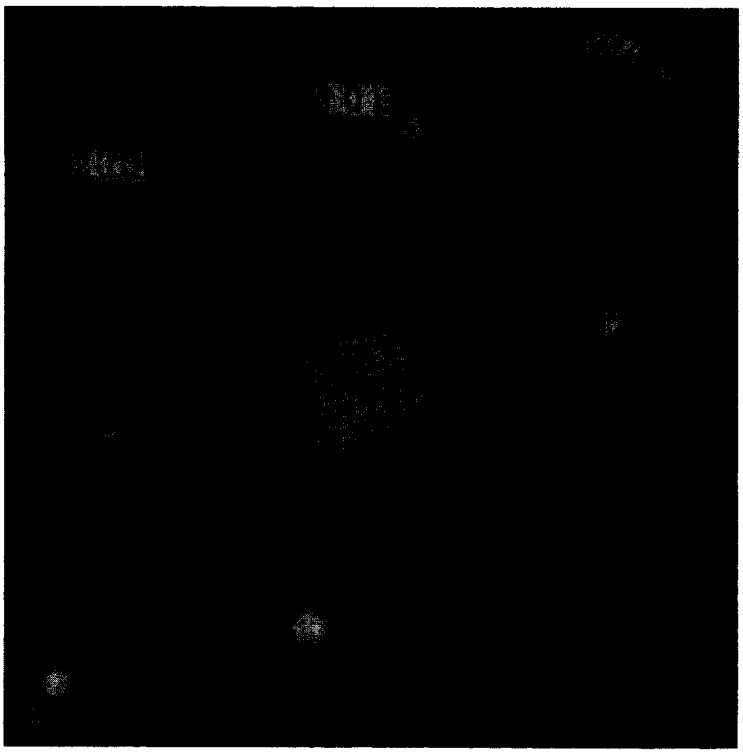

FIG. 2. (a) Electron diffraction pattern for an $(020)_r$ superstructure ($D_{sp} = 25.9$ Å) showing diffuse streaking parallel to $g(020)_r$. (b) Electron diffraction pattern for a twinned, $(0kl)_r$ superstructure ($D_{sp} = 39.0$ Å). Here the diffuse intensity is streaked parallel to the twinned superstructure directions $g(0kl)_r$ and $g(0k\bar{l})_r$. (c) $[010]_r$ zone axis pattern. The reciprocal lattice section is perpendicular to the direction of diffuse streaking which thus intersects the section in a series of sharp spots, marked A. These form a $(101)_r$ superlattice with a periodicity of $4.6 \times d_{(101)_r}$. Weaker, more diffuse spots directed along $g(10\bar{1})_r$ are also apparent (B).

expected for $(020)_r$ superstructures. Figure 2b shows the same rutile zone as for Fig. 2a. Here the superlattice spacing along $g(020)_r$ is 30.0 Å, which indicates that the superstructure has swung away from $(020)_r$ towards $(031)_r$, and in fact the sharp superlattice spots are now seen to be inclined to $g(020)_r$ in a twin configuration. As in Fig. 2a, the diffuse streaking lies parallel to the superlattice directions; i.e., pairs of diffuse streaks parallel to the $g(0kl)_r$ and $g(0k\bar{l})_r$ superlattice directions intersect at approximately 30°. That the diffuse intensity was in the form of streaks, rather than sheets, was confirmed by tilting crystals into the $[010]_r$ zone which is orthogonal to Figs. 1a and 1c. The diffuse streaks of Fig. 2a are now normal to the Ewald sphere and appear as relatively sharp spots (A) defining a superlattice periodicity along $g(101)_r$. The periodicity varies from 4.25 to $4.69 \times d_{101_r}$ for different crystal flakes. A further set of weak diffuse spots also occur (B) along $g(10\bar{1})_r$ (Fig. 2c).

In our initial single-crystal X-ray studies we found no evidence of weak reflections signifying a superstructure for directions other than along $g(020)_r$. However, following the observation of diffuse scattering in the electron diffraction patterns we studied a number of single crystals by the precession method, using very long exposures, and obtained the same result. For the data collection crystal in particular, photographs exposed for 100 hr showed the same $4.5 \times d_{101_r}$ superlattice reflections as found by electron diffraction. These weak spots had intensities of the order

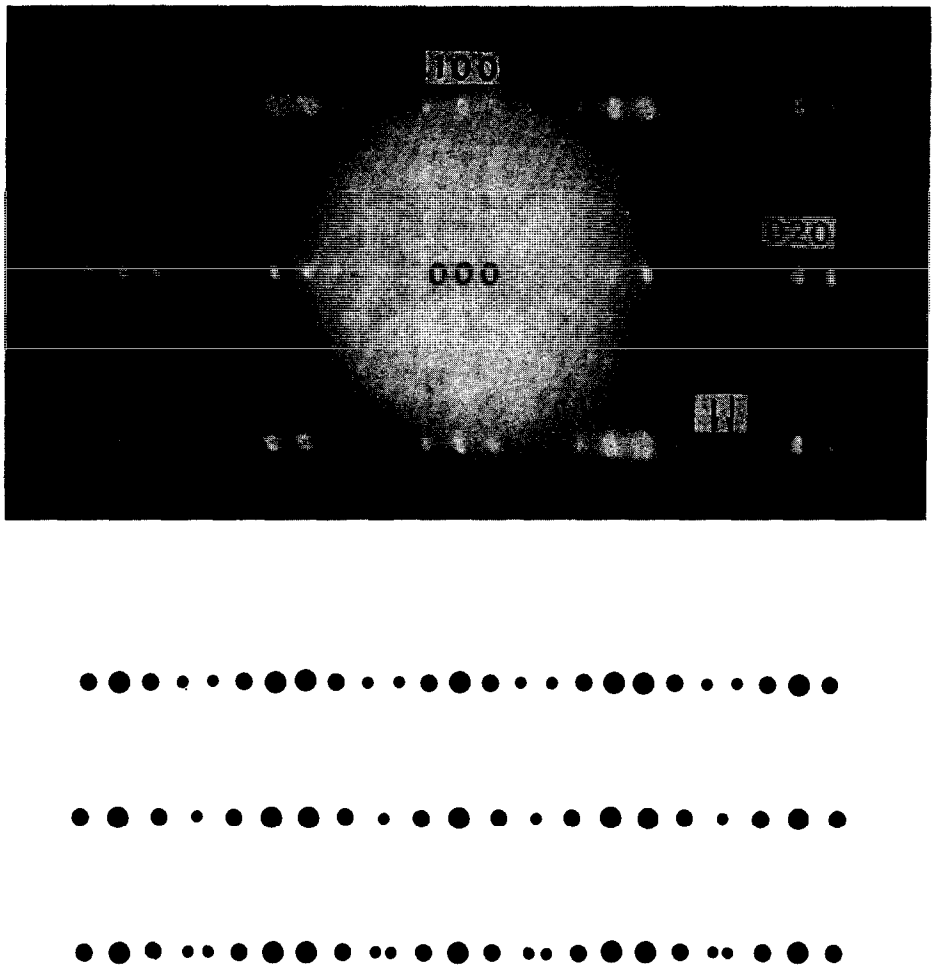

FIG. 3. [001]$_r$ zone axis photograph of an (020)$_r$ superstructure, displaying a spacing anomaly along g(020)$_r$ (marked with arrows). Calculated intensities for the (1k0)$_r$ lattice row are shown for (i) 11 × $d_{(010)_r}$ superstructure, (ii) 9 × $d_{(010)_r}$ superstructure, (iii) 9× + 11× intergrowth structure.

of one-hundredth that of the sharp (020)$_r$ supercell reflections.

4. Structure Analysis

A single crystal was carefully selected to ensure that the superlattice rows were exactly along g(020)$_r$. Precession photographs showed a small spacing anomaly along g(020)$_r$ of the type shown in Fig. 3. From a least-squares refinement of accurately centered diffractometer reflections, a unit cell repeat of 144.9 Å was obtained (see Section 4.2), corresponding to an *average CS* plane separation of 10.33 × $d_{(020)_r}$. In view of the obvious difficulties associated with obtaining a meaningful structure analysis with such a large unit cell and the limited amount of intensity data available, we decided to work initially under the approximation that the *CS* spacing was 11 × $d_{(020)_r}$, i.e., an integral multiple. This approach has been used successfully by Koch and Cohen to obtain the average structure for wustite (*6*). The average structure could then be modified to include, firstly, the nonintegral superlattice along g(020)$_r$, and secondly diffuse scattering.

Both these diffraction effects may be considered to result from long-range disorder variations of a local arrangement of atoms; i.e., the spacing anomalies are due to long-range periodic variations in the superlattice repeat along $[010]_r$, and the diffuse streaking, especially that parallel to $[010]_r$, may be interpreted as due to the breakdown of long-range ordering of $(010)_r$ planes.

4.1. Determination of the Average Structure

The unit cell assigned to the short-range ordered or average structure is orthorhombic with

$$a = 4.618(5)\ \text{Å} \simeq a_r\ (= 4.5937\ \text{Å})$$

$$b = 51.36(5)\ \text{Å} \simeq 11 \times b_r\ (= 50.53\ \text{Å})$$

$$c = 2.953(3)\ \text{Å} \simeq c_r\ (= 2.9581\ \text{Å}).$$

For the $11\times$ supercell, three possible space groups are consistent with the observed systematic extinctions. These are *Amam*, *Ama2*, and $A2_1am$. The first two may be excluded on the ground that the rutile substructure cannot be formed using them; instead, mirror planes at $x = \frac{1}{4}$ generate NiAs-type strings from atoms placed at $x = 0$.

A trial model was constructed in space group $A2_1am$, comprising rutile slabs infinitely extended along [100] and [001] but displaced relative to one another by $\frac{1}{2}[011]_r$, the displacement vector of the low temperature $(hkl)_r$ *CS* structure precursor. All atoms were placed in position $4a$ of space group $A2_1am$, i.e., $xy0$, etc., with one metal atom $M(1)$ at $(0, y, 0)$ to fix the origin. The symmetry operations repeat $M(1)$ at $(\frac{1}{2}, y, 0)$, resulting in strings of metals separated by $\frac{1}{2}a = 2.31$ Å at the *CS* plane. To prevent this structurally unlikely situation we initially set the occupancy of site $M(1)$ at two-thirds and allowed the parameter to vary in the refinement. All other atoms were initially set at idealized positions defined by the rutile substructure. Some difficulty was encountered in the subsequent refinement of atoms because of the strong correlations involved. However, a satisfactory convergence was achieved, resulting in a final R factor of 0.09 and a weighted R of 0.079. The final parameters, with their standard deviations, are given in Table I.

TABLE I

POSITIONAL AND THERMAL PARAMETERS FOR THE $11 \times (020)_r$ SUPERSTRUCTURE

Atom	x	y	z	B (Å^2)
$M(1)$	0.0000	0.0053(2)	0	0.14(9)
$M(2)$	−0.0302(20)	0.0942(2)	0	0.54(15)
$M(3)$	0.0011(23)	0.1832(2)	0	−0.08(11)
$M(4)$	−0.0022(43)	0.2726(3)	0	1.04(11)
$M(5)$	0.0135(19)	0.3618(2)	0	0.38(18)
$M(6)$	−0.0433(19)	0.4511(2)	0	0.64(13)
O(1)	0.2809(70)	0.0316(6)	0	0.70(40)
O(2)	0.1923(84)	0.5773(7)	0	0.42(53)
O(3)	0.2906(86)	0.1195(6)	0	0.06(53)
O(4)	0.1923(46)	0.6649(4)	0	−0.17(24)
O(5)	0.2882(81)	0.2103(6)	0	0.44(57)
O(6)	0.1870(138)	0.7565(12)	0	1.00(24)
O(7)	0.2991(114)	0.2996(11)	0	−0.07(78)
O(8)	0.2381(88)	0.8494(7)	0	1.56(69)
O(9)	0.3100(114)	0.3883(8)	0	0.20(69)
O(10)	0.2221(70)	0.9353(6)	0	0.51(39)
O(11)	0.2760(73)	0.4809(6)	0	1.40(60)

From the refinement, the occupancy factor for site $M(1)$ was determined to be 0.70 ± 0.05. This value was obtained in a refinement in which the temperature factor for $M(1)$ was set at the average for the other metals. It is apparent that the individual isotropic temperature factors, which have large associated errors, have no real physical meaning. This is partly a result of the very limited data set, in which more than four-fifths of the measured independent reflections had intensities close to zero. It also partly reflects our approximation of the real structure by an average structure model defined by the $11\times$ supercell. Despite the above limitations, we believe our average structure approach is justified by the satisfactory refinement of the model and the crystallochemically reasonable values obtained for the bond distances (see Table II).

A (100) section of the structure, with the oxygen layer idealized to hexagonal close packing, is shown in Fig. 4a. The refined structure is shown projected along [001] in Fig. 5. The metal atoms occupying the face-shared octahedral sites $M(1)$ and their octahedrally coordinated anions are outlined

TABLE II

BOND DISTANCES FOR THE 11× SUPERSTRUCTURE

M(1) Octahedron		*M*(2) Octahedron		*M*(3) Octahedron		*M*(4) Octahedron		*M*(5) Octahedron		*M*(6) Octahedron	
					Metal–oxygen (Å)						
M(1)–O(1)	1.88(4)	*M*(2)–O(2)	1.99(3)	*M*(3)–O(4) × 2	1.96(3)	*M*(4)–O(5) × 2	1.97(3)	*M*(5)–O(3) × 2	2.04(3)	*M*(6)–O(1) × 2	1.90(2)
–O(1′)	2.16(4)	–O(3)	1.97(4)	–O(5)	1.93(4)	–O(6) × 2	1.90(4)	–O(4)	2.02(4)	–O(2)	1.90(4)
–O(11) × 2	1.93(2)	–O(9) × 2	1.87(3)	–O(7) × 2	1.96(4)	–O(6′)	2.07(6)	–O(8) × 2	1.91(3)	–O(10) × 2	2.08(2)
–O(11′) × 2	2.32(3)	–O(10) × 2	1.90(3)	–O(8)	2.06(4)	–O(7)	1.97(6)	–O(9)	1.96(5)	–O(11)	2.14(4)
					Oxygen–oxygen (Å)						
O(1)–O(11) × 2	2.83(5)	O(2)–O(2′)	2.95	O(4)–O(4)	2.95	O(5)–O(5)	2.95	O(3)–O(3)	2.95	O(1)–O(1)	2.95
O(1)–O(11′) × 2	3.00(5)	O(2)–O(3) × 2	2.66(4)	O(4)–O(5) × 2	2.80(4)	O(5)–O(6) × 2	2.51(7)	O(3)–O(4) × 2	2.79(4)	O(1)–O(2) × 2	2.80(5)
O(1′)–O(11) × 2	3.00(5)	O(2)–O(9) × 2	2.47(6)	O(4)–O(7) × 2	2.58(6)	O(5)–O(6′) × 2	2.83(6)	O(3)–O(8) × 2	2.61(5)	O(1)–O(10) × 2	2.64(5)
O(1′)–O(11′) × 2	2.81(5)	O(2)–O(10) × 2	2.70(4)	O(4)–O(8) × 2	2.67(5)	O(6)–O(6′) × 2	2.82(8)	O(3)–O(9) × 2	2.88(6)	O(1)–O(11) × 2	2.80(5)
O(11)–O(11)	2.95	O(3)–O(9) × 2	2.66(5)	O(5)–O(7) × 2	2.75(5)	O(6)–O(7) × 2	2.71(7)	O(4)–O(8) × 2	3.01(5)	O(2)–O(10) × 2	2.93(4)
O(11)–O(11′) × 2	3.03(6)	O(9)–O(9)	2.95	O(7)–O(7)	2.95	O(5)–O(7) × 2	2.83(5)	O(8)–O(8)	2.95	O(10)–O(10)	2.95
O(11′)–O(11′)	2.95	O(9)–O(10)	2.87(4)	O(7)–O(8)	2.97(6)	O(6)–O(6)	2.95	O(8)–O(9) × 2	2.51(4)	O(10)–O(11) × 2	2.79(4)
					Metal–metal (Å)						
M(1)–*M*(1′)(f)[a]	2.37	*M*(2)–*M*(2′)(e)	2.95	*M*(3)–*M*(3′)(e)	2.95	*M*(4)–*M*(4′)(e)	2.95	*M*(5)–*M*(5′)(e)	2.95	*M*(6)–*M*(6′)(e)	2.95
–*M*(1″)(e)	2.95	–*M*(5)(c)	3.43	–*M*(4)(c)	3.55	–*M*(3)(c)	3.55	–*M*(2)(c)	3.43	–*M*(1)(e)	3.16
–*M*(6)(e)	3.16			–*M*(5)(c)	3.55	–*M*(4′)(c)	3.59	–*M*(2′)(c)	3.69	–*M*(1′)(c)	3.41
–*M*(6)(c)	3.41	–*M*(6)(c)	3.55	–*M*(4′)(c)	3.57	–*M*(3′)(c)	3.57	–*M*(3)(c)	3.55	–*M*(2)(c)	3.55
–*M*(6′)	3.67	–*M*(6)(c)	3.63	–*M*(7′)(c)	3.63					–*M*(2)(c)	3.63

[a] Letters c, e, and f refer to corner, edge, and face-sharing, respectively.

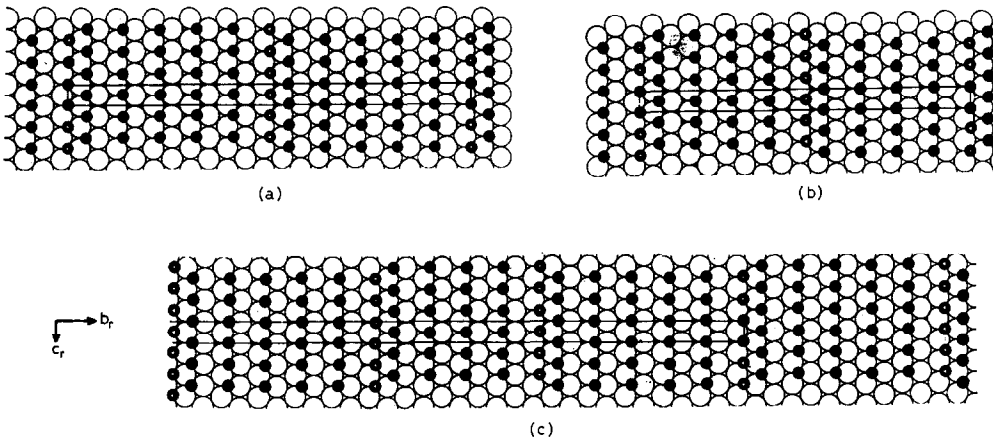

FIG. 4. Idealized $(100)_r$ sections of $(020)_r$ superstructures. (a) 11× superstructure, (b) 9× superstructure, (c) $2\cdot(11\times)+(9\times)$ intergrowth. Unit cell outlines are shown.

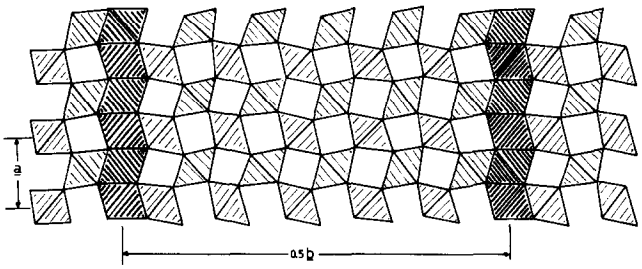

FIG. 5. An $[001]_r$ section of the actual structure determined for the 11× superstructure. Oxygen atoms are at the vertices of the shaded octahedra; metal atoms are not shown. The lightly shaded octahedra form blocks of rutile type structure and are separated by layers of deficient nickel arsenide structure, shown in heavy shading.

by heavy shading in the diagram. The [100] strings of $M(1)O_6$ octahedra link by edge-sharing along [001] to form sheets parallel to $(020)_r$. Adjacent slabs of rutile structure are displaced by $\frac{1}{2}[011]_r$ across these planar boundaries. Since the shaded $M(1)O_6$ octahedra (Fig. 5) are only about two-thirds occupied the structure cannot be formally described as an $(020)_r$-$\frac{1}{2}[011]_r$ *CS* plane structure. Application of this operation on every twelfth oxygen-only $(020)_r$ plane gives a structure topologically similar to that shown in Figs. 4 and 5 but with *full* occupation of available octahedral sites in the $(020)_r$ *CS* planes. In this case, adjacent rutile slabs would be separated by MO slabs of NiAs-type structure. Reducing the occupancy factor to two-thirds would mean that, on the average, each MO_6 octahedron shares only one face, and the stoichiometry at the *CS* plane would be M_2O_3.

From the refined occupancy factor of $M(1)$ sites, we can calculate a composition for the $(020)_r$ superstructure of $M_{5.7}O_{11}$, i.e., $MO_{1.930}$, $M = (\text{Ti, Fe})$. This may be expressed as approximately $Fe_2O_3 + 12TiO_2$ $(MO_{1.929})$, although the presence of some FeO will modify the formula slightly. The calculated percentage by weight of Fe_2O_3 is 14.3, in good agreement with the phase analysis, and the calculated 85.7 wt% TiO_2 consistent with the value of approximately 90 wt% measured from MacChesney and Muan's phase diagram for the limit of rutile solid solution at 1550°C. (Low resolution Debye–Scherrer photographs do not readily discriminate between rutile and the rutile-derived superstructures.)

Of course, the 11× superstructure is just one member of a family of structures based on the *CS* operation $\frac{1}{2}[011]_r(020)_r$. With full occupancy of $M(1)$ sites the 11× superstructure would be M_6O_{11}, i.e., $n=6$ in a M_nO_{2n-1} homologous series. The next lowest member, with $n=5$, is shown in Fig. 4b. This may be produced by removal of every tenth oxygen-only $(020)_r$ plane followed by collapse and slip by the vector $\frac{1}{2}[011]_r$. Other members of the family may be produced by removing one oxygen plane in $2n$.[1] Note that the $n=5$ homolog will give rise to a 9× superlattice out to 020_r, and in general there will be $2n-1$ spots. In reality, the family is more precisely described by the formula $M_{n-\delta}O_{2n-1}$, where we have determined $\delta = 0.30 \pm 0.05$ for $n=6$. Further discussion of the structural consequences of fractional occupancy will be postponed until Section 4.3.

4.2. Parallel Intergrowth of the 11× and 9× Superstructure

(a) Refinement of the cell parameters. Figure 3 shows a spacing anomaly for a $(020)_r$ superstructure. Calculated $1k0$ lattice rows are given in Fig. 3 for (i) an 11×, (ii) a 9×, and (iii) an ordered intergrowth of 11× + 9× superstructures. Note the correspondence between the observed diffraction pattern and Fig. 3(iii). We have measured the superlattice reflection positions carefully for a number of crystals showing $(020)_r$ superstructures. All gave spot positions intermediate between those expected for 11× and 9× superstructures. We interpret these as parallel intergrowths of the simple $n=6$ and $n=5$ homologs. A 10× superstructure is thus a 1:1 intergrowth.

For the crystal used in the structure analysis we obtained a set of 37 accurately centered reflection positions (see Table III.b). Table III.a shows the unit cell values obtained by least-squares fits of the data for cells based on an 11× supercell, and three different intergrowths $P\cdot(11\times)+Q\cdot(9\times)$. The combined lattice parameter errors are given as percentage errors in the unit cell volume. Relatively poor fits result for the 11× and 11× + 9× cells. The percentage errors for the $2(11\times)+(9\times)$ and $5(11\times)+2(9\times)$ cells are equal, and only half that for an assumed 1:1 intergrowth. Assuming the same fractional occupancy of the $M(1)$ sites as determined for the 11× superstructure, the calculated compositions for the latter two intergrowths are $(Ti, Fe)O_{1.9248}$ and $(Ti, Fe)O_{1.9255}$. Thus, we are unable to detect composition variations $MO_{x+\delta x}$ having $\delta x \sim 0.001$. Interestingly, we found the same limit of resolution, using least-squares refinement of X-ray data, for x in $Ba_{1+x}Fe_2S_4$ (*7*). In Table III.b is shown a comparison of observed $\sin^2\theta$ values with those calculated for the smaller of the "best fit" cells, i.e., $2(11\times)+(9\times)$.

(b) Structure factor calculations for a $2\cdot(11\times)+1\cdot(9\times)$ intergrowth. We considered (Section 4.1) the 11× superstructure as a first

[1] Note that this is a formal operation only. In a reaction between Fe_2O_3 and TiO_2 it is more likely that the $(020)_r$ metal-deficient *CS* plane is formed by metal diffusion, and it is not necessary to have any anion vacancies as such. In fact, the observation of metal-deficient *CS* planes almost certainly precludes the presence of anion vacancies.

TABLE III.a

LATTICE PARAMETERS FOR DIFFERENT INTERGROWTHS OBTAINED BY LEAST-SQUARES REFINEMENT OF THE SINGLE-CRYSTAL DIFFRACTOMETER DATA

	a (Å)	b (Å)	c (Å)	V (Å^3)
11 × $(010)_r$ superstructure, $(Ti, Fe)O_{1.9200}$	4.618 ± 0.005	51.361 ± 0.057	2.953 ± 0.003	700.41(±0.32%)
11× + 9× intergrowth, $(Ti, Fe)O_{1.9223}$	4.618 ± 0.004	93.527 ± 0.076	2.953 ± 0.002	1275.42(±0.23%)
$2(11\times)+9\times$ intergrowth, $(Ti, Fe)O_{1.9248}$	4.618 ± 0.002	144.888 ± 0.065	2.953 ± 0.001	1975.83(±0.12%)
$5(11\times)+2(9\times)$ intergrowth, $(Ti, Fe)O_{1.9255}$	4.618 ± 0.002	341.136 ± 0.155	2.953 ± 0.001	4198.74(±0.12%)

TABLE III.b

COMPARISON OF SINGLE CRYSTAL DIFFRACTOMETER DATA WITH CALCULATED DATA FOR THE 2(11×) + 9× INTERGROWTH (SEE TABLE III.a)

	$\sin^2\theta$	
h k l	Observed	Calculated, for 2(11×) + 9× intergrowth
0 0 2	0.05775	0.05790
0 0 4	0.23170	0.23163
0 56 0	0.01882	0.01886
0 62 0	0.02311	0.02312
0 68 0	0.02778	0.02781
0 124 0	0.09228	0.09248
0 130 0	0.10142	0.10165
0 180 0	0.19516	0.19488
0 186 0	0.20808	0.20809
0 192 0	0.22172	0.22173
0 254 0	0.38824	0.38806
0 25 1	0.01823	0.01823
0 31 1	0.02024	0.02025
0 37 1	0.02272	0.02271
0 87 1	0.05981	0.06000
0 93 1	0.06645	0.06650
0 99 1	0.07330	0.07343
0 155 1	0.15871	0.15898
0 161 1	0.17025	0.17039
0 56 2	0.07662	0.07677
0 62 2	0.08076	0.08103
0 124 2	0.15030	0.15039
0 130 2	0.15940	0.15956
0 186 2	0.26618	0.26600
0 192 2	0.27959	0.27964
0 31 3	0.13617	0.13607
0 93 3	0.18229	0.18231
0 99 3	0.18922	0.18924
0 161 3	0.286366	0.28620
0 62 4	0.25480	0.25475
1 28 0	0.01067	0.01063
1 34 0	0.01293	0.01287
1 62 0	0.02903	0.02904
1 3 1	0.02049	0.02045
1 31 1	0.02623	0.02617
2 0 0	0.02372	0.02368
4 0 0	0.09470	0.09472

approximation to the structure of a crystal of the high-temperature (020)$_r$ phase. Refinement of this model gave accurate values for the position coordinates for the *local* atom ordering in both the rutile-like and the *CS* plane regions of the structure. We now combine this information with a more precise measurement of the supercell (Section 4.2(a) above) to more closely approach the real crystal structure. A diagram of the $2\cdot(11\times) + 1\cdot(9\times)$ intergrowth, with an overall repeat of $31 \times b_r$, is given in Fig. 4c. It has the same A centered orthorhombic symmetry as the 11× structure. The single-crystal intensity data were reindexed using this new unit cell and structure factors were calculated using atomic positions scaled directly from the refined positions for the 11× cell. No attempt was made to refine the intergrowth structure because of the large number of variables (145) for only 451 independent reflections. Despite this, an unrefined R factor of 0.10 was obtained, verifying that the model is quite close to the crystal structure. We assumed the same occupancy factor 0.70 for the $M(1)$ sites as for the 11× superstructure. In fact, this should be slightly smaller for the larger cell, where the average *CS* plane spacing is smaller, but this could not be confirmed owing to the inadequacy of the intensity data.

(*c*) *Limitations to the accuracy of the intergrowth model.* Owing to small inhomogeneities in the sample mixtures and small temperature variations during equilibration, a crystal, such as the one studied above, could contain microlamellae of many high-order intergrowths. These would not be separately resolved by X-ray diffraction if the composition range was less than $\delta x \sim 0.002$. For example, a $5\cdot(11\times) + 2\cdot(9\times)$ intergrowth has stoichiometry (Ti, Fe)$O_{1.9255}$ and could coexist with a $2\cdot(11\times) + 1\cdot(9\times)$ intergrowth, stoichiometry (Ti, Fe)$O_{1.9248}$, without being detected. High-resolution electron microscopy structure images are necessary to determine the extent of inhomogeneity of our single crystals.

A second, more fundamental, structural problem is that for high-order intergrowths (i.e., for P and/or $Q \geqslant 2$) there are $(P + Q - 1)!/(P!(Q - 1)!)$ possible sequences for intergrowing P slabs of 11× and Q slabs of 9× superstructure. These may be easily interconverted by fixing the width of the first slab in a sequence and rearranging the remaining $(P + Q - 1)$ slabs by simple diffusive hops of metal atoms. If identical hops

occur in *each* unit cell then each of the possible structures has the same unit cell dimensions. For example, for the $P = 5$, $Q = 2$ intergrowth the possible sequences of $n = 6$ and $n = 5$ structures are

$$\ldots 6\,6\,6\,6\,6\,5\,5\,6\,6\,6\,6\,6\,5\,5\ldots \quad (1)$$
$$\ldots 6\,6\,6\,6\,5\,6\,5\,6\,6\,6\,6\,5\,6\,5\ldots \quad (2)$$
$$\ldots 6\,6\,6\,5\,6\,6\,5\,6\,6\,6\,5\,6\,6\,5\ldots \quad (3)$$
$$\ldots 6\,6\,5\,6\,6\,6\,5\,6\,6\,5\,6\,6\,6\,5\ldots \quad (4)$$
$$\ldots 6\,5\,6\,6\,6\,6\,5\,6\,5\,6\,6\,6\,6\,5\ldots \quad (5)$$

All of these have identical unit cell dimensions. Sequences (2) and (5) are equivalent after a shift in origin, so that these two will give identical diffracted intensities; and similarly for sequences (3) and (4), leaving three possible structures which should give different intensity distributions of diffracted intensity over the same set of reciprocal lattice points. Structure factor calculations were made for two of the sequences, (1) and (3). Only the metal atoms were included in the calculation, and local atomic distortions were allowed for by scaling the refined atomic positions for the $11\times$ cell. Computed F^2_{0kl} values are shown in Table IV. Three orders of diffraction effects are apparent. Strongest is the rutile subcell reflection with $d^* = 1/b_r$. Next in intensity are superstructure reflections corresponding to an *averaged* periodicity, $d^* = 1/(10.43 \times b_r)$, where $10.43 \times b_r = (5 \times 11b_r + 2 \times 9b_r)/7$. Finally, arranged about the superstructure reflections are "super-superstructure" reflections, using the terminology of Mann and Bevan (*8*). These have periodicity $d^* = 1/(73 \times b_r)$, being the overall repeat of the high-order intergrowth. Table IV shows that the intergrowth sequences have almost identical distribution of subcell and supercell reflection intensities, but quite different super-superlattice intensities, and it is the latter which must be used to identify a particular intergrowth sequence.

Careful inspection of X-ray and electron single-crystal diffraction patterns failed to show any super-superstructure reflections, even though these should be easily resolvable from the superstructure spots. A similar problem was encountered with parallel intergrowth sequences of V_3O_5-type and α-PbO_2-type structures in the $MO_{\sim 1.77}$ region of the $Cr_2O_3 + Fe_2O_3 + TiO_2 + ZrO_2$ system (*9*). In that case it was concluded that there was maximum alternation of the two components. This corresponds to sequence (3), or (4), in the present problem. (It also corresponds to the case of "uniform mixing" found by Fujiwara (*10*) for mixtures of different superlattice spacings in some metal alloys.) It appears that for our crystals there is a complex statistical assemblage of intergrowth sequences, with contributions from both stoichiometry inhomogeneity and from long-range disorder for the high-order intergrowths, smearing super-superstructure into the background. Again, it is likely that high-resolution electron microscope images will clarify this problem. Table IV also shows that for different intergrowths, the positions of supercell reflections coincide when they are adjacent to subcell reflections, but with increasing distance from the subcell reflection, the positions of the supercell reflections diverge. Thus, for a disordered crystal containing a number of spacings, the supercell reflections will be more smeared out as their distance from the subcell reflection increases. This is in fact observed in Fig. 1, where it will be seen that the supercell rows are limited to one or two reflections on either side of the subcell reflections.

4.3. Metal Atom Ordering in the CS Planes

In the structure refinement (Section 4.1) it was necessary to assign fractional occupancy to $M(1)$ metal atom sites in the *CS* planes, but it was not possible to order the metals in a way which would be consistent with the observed symmetry and unit cell dimensions. However, diffuse streaks were observed on the electron diffraction patterns (Fig. 2). The observation that the diffuse scattering is elongated parallel to the superlattice direction, and that a relatively sharp $4.5 \times d_{101}$ supercell was found for the $(010)_r$ reciprocal section (Fig. 2c), suggests that there is quite well-defined ordering of the metal atoms within each *CS* plane but there is no, or very little, correlation of this ordering between adjacent *CS* planes. Imperfect regularity in the *CS* plane spacings may partly account for this. We made a number of attempts to construct

TABLE IV

CALCULATED STRUCTURE FACTORS (SQUARED) FOR TWO (020), INTERGROWTH SEQUENCES WITH THE SAME PERIODICITY

h k l	F^2 for 5(11×)–2(9×)–5(11×)–		F^2 for 3(11×)–9×–2(11×)–9×–3(11×)–	
0 1 1	*		*	
0 3 1	*		*	
0 5 1	*		*	
0 7 1	2.4	Supercell	2.5	
0 9 1	*		*	
0 11 1	*		*	
0 13 1	*		*	
0 15 1	*		*	
0 17 1	*		*	
0 19 1	*		*	
0 21 1	1.5	Supercell	2.4	
0 23 1	*		*	
0 25 1	*		*	
0 27 1	*		*	
0 29 1	*		*	
0 31 1	*		*	
0 33 1	2.2	Supercell	*	
0 35 1	*		2.3	
0 37 1	*		*	
0 39 1	*		*	
0 41 1	*		*	
0 43 1	*		*	
0 45 1	2.1	Supercell	5.0	
0 47 1	4.1		*	
0 49 1	*		2.0	
0 51 1	*		*	
0 53 1	*		*	
0 55 1	*		1.0	
0 57 1	2.1		*	
0 59 1	Super-supercell 19.8	Supercell	26.0	Super-supercell
0 61 1	4.2		*	
0 63 1	*		1.2	
0 65 1	*		*	
0 67 1	*		*	
0 69 1	*		1.0	
0 71 1	2.3		*	
0 73 1	2427.5	Subcell	2422.0	
0 75 1	2.1		*	
0 77 1	*		1.1	
0 79 1	*		*	
0 81 1	*		*	
0 83 1	*		*	
0 85 1	3.0		*	
0 87 1	20.8		27.0	
0 89 1	1.3		*	
0 91 1	*		*	
0 93 1	*		*	
0 95 1	*		*	
0 97 1	*		1.0	
0 99 1	1.5		*	

* An asterisk signifies $F^2 < 1$.

ordered arrangements of metals in the $M(1)$ sites that would be consistent with the $4.5 \times d_{101}$ superlattice. Various configurations, such as that which occurs in corundum (or α-Fe_2O_3) giving two-thirds occupancy, give reasonable intensities, but we have not been able to reproduce the spot positions. One difficulty here is the uncertainty in the occupancy factor, 0.70 ± 0.05, which would allow such fractions as $\frac{2}{3}$, $\frac{7}{10}$, and $\frac{3}{4}$.

The fractional (variable) superlattice repeat also indicates that we have another intergrowth problem. In the absence of accurate intensity measurements of the diffuse scattering it is therefore clearly not feasible to establish the metal-atom ordering within the *CS* planes at this stage.

5. Conclusion

By using an intimate combination of electron and X-ray diffraction techniques it has proved possible to establish the structural principles of the $(020)_r$ superstructures. This study has further demonstrated the complementary nature of the two techniques, both techniques being subject to errors if used in isolation.

The composition region TiO_2 plus 14–16 wt% Fe_2O_3 is spanned by a continuous series of intergrowths, parallel to $(020)_r$, of two rutile related *CS* structures, designated 11× and 9× superstructures. These are metal-deficient homologs of a hypothetical $(020)_r$ *CS* family derived from rutile by the *CS* operation $\frac{1}{2}[011]_r(020)_r$. The family may be written $M_{n-\delta}O_{2n-1}$, where n has values of 5 and 6 for the 9× and 11× superstructures and $\delta = 0.30 \pm 0.05$ for the $n = 6$ member.

For the temperature range of our study, the equilibrium phases are within 20°C of their melting points, and this is reflected in the incompleteness of structural order. The results show both long-range disorder in the intergrowth sequences and also an absence of correlation in the metal atom ordering at the *CS* planes from one *CS* plane to the next. The intergrowths $P\cdot(11\times) + Q\cdot(9\times)$ ranged from $P = 1$, $Q = 0$ (the 11× end member) to approximately $P = 1$, $Q = 2$. The corresponding range of observed *CS* plane spacings was 25.71–22.59 Å, and the calculated composition range was $MO_{1.9298}$ to $MO_{1.9199}$.

At temperatures below 1450°C the $(020)_r$ intergrowths transform to ordered $(121)_r$ *CS* structures. A similar reversible structural transformation was observed in the Cr_2O_3–TiO_2 system by Flörke and Lee (*11*). Presumably the low- to high-temperature transformation is accompanied by some reduction of Fe^{3+}, and so the low-temperature precursors will have compositions slightly higher than the range given above. Interestingly, $(121)_r$ *CS* structures M_nO_{2n-1}, with $n = 14$–16, i.e., $MO_{1.9286}$ to $MO_{1.9375}$, have *CS* plane spacings of 23.03 and 26.39 Å (using the formula $D_{sp} = d_{121}(n - 0.347)$; Ref. (*12*)). Thus, the low–high temperature transformation involves a cooperative reorientation of the *CS* planes from $(121)_r$ to $(020)_r$, while the *CS* plane spacing remains almost constant.

Consideration of reaction mechanisms for the structural transformation must include the observation that at temperatures close to 1450°C the $(121)_r$ *CS* structures are always very finely polysynthetically twinned (*2*, *13*, *14*). At least in principle, it is possible to construct $(020)_r$ boundaries by ordered intergrowth of various $\{121\}_r\frac{1}{2}\langle 011\rangle_r$ *CS* structures. For example, $(121)_r\frac{1}{2}[0\bar{1}1]_r + (\bar{1}2\bar{1})_r\frac{1}{2}[01\bar{1}]_r = 2(020)_r\frac{1}{2}[011]_r$, or, if three twin orientations are present, $(121)_r\frac{1}{2}[0\bar{1}1]_r + (\bar{1}21)_r\frac{1}{2}[0\bar{1}1]_r + 2(12\bar{1})_r\frac{1}{2}[0\bar{1}\bar{1}]_r = 4(020)_r\frac{1}{2}[011]_r$. Note that all four vectors $\frac{1}{2}[011]_r$, $\frac{1}{2}[0\bar{1}1]_r$, $\frac{1}{2}[0\bar{1}1]_r$, and $\frac{1}{2}[0\bar{1}\bar{1}]_r$ produce exactly equivalent *CS* planes when operating across $(020)_r$, or $(0\bar{2}0)_r$, planes. They differ only by a lattice vector parallel to the *CS* plane. At 1300°C the twin lamellae are 500–1000 Å wide, but at higher temperatures, approaching the transformation temperature, the twin lamellae diminish in width. It is tempting to suggest that if a point is reached where the twin bands are smaller than the *CS* plane spacing then the twinning will initiate a structural change at the unit cell level. Such a transformation would be reversible, as observed. However, much more detailed electron microscopy, using samples quenched from around the transformation temperature, is needed before a detailed model for the reaction mechanism can be constructed.

Acknowledgments

The authors express their gratitude to Mrs. C. Li for assistance in preparations and analyses and to Dr. J. Ward for obtaining Mössbauer spectra for the samples.

References

1. L. A. BURSILL, *J. Solid State Chem.* **10**, 72 (1974).
2. L. A. BURSILL AND B. G. HYDE, *Progr. Solid State Chem.* 7, 177 (1972).
3. L. A. BURSILL, I. E. GREY, AND D. J. LLOYD, *in* "Diffraction Studies of Real Atoms and Real Crystals" (Abstracts of Papers Presented at the International Crystallography Conference, Melbourne, August, 1974), Abstract II N-5, Australian Academy of Science, 1974.
4. J. B. MACCHESNEY AND A. MUAN, *Amer. Mineral.* **44**, 926 (1959).
5. J. HORNSTRA AND B. STUBBE, "PW1100 Data Processing Program," Philips Research Lab., Eindhoven, 1972.
6. F. KOCH AND J. B. COHEN, *Acta Crystallogr., Sect. B.* **25**, 275 (1969).
7. I. E. GREY, *J. Solid State Chem.* **11**, 128 (1974).
8. A. W. MANN AND D. J. M. BEVAN, *J. Solid State Chem.* **5**, 410 (1972).
9. I. E. GREY, A. F. REID, AND J. G. ALLPRESS, *J. Solid State Chem.* **8**, 86 (1973).
10. K. FUJIWARA, *J Phys. Soc. Japan* **12**, 7 (1957).
11. O. W. FLÖRKE AND C. W. LEE, *J. Solid State Chem.* **1**, 445 (1970).
12. L. A. BURSILL, B. G. HYDE, O. TERASAKI, AND D. WATANABE, *Philos. Mag.* **20**, 347 (1969).
13. O. TERASAKI AND D. WATANABE, *Jap. J. Appl. Phys.* **10**, 292 (1971).
14. R. M. GIBB AND J. S. ANDERSON, *J. Solid State Chem.* **5**, 212 (1972).